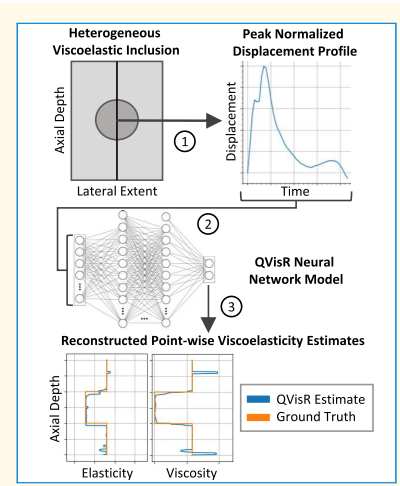


# Quantitative Viscoelastic Response (QVisR): Direct Estimation of Viscoelasticity With Neural Networks

Joseph B. Richardson<sup>®</sup>, *Student Member, IEEE*, Christopher J. Moore, *Member, IEEE*, and Caterina M. Gallippi<sup>®</sup>, *Senior Member, IEEE* 

Abstract—We present a machine learning method to directly estimate viscoelastic moduli from displacement time-series profiles generated by viscoelastic response (VisR) ultrasound excitations. VisR uses two colocalized acoustic radiation force (ARF) pushes to approximate tissue viscoelastic creep response and tracks displacements on-axis to measure the material relaxation. A fully connected neural network is trained to learn a nonlinear mapping from VisR displacements, the push focal depth, and the measurement axial depth to the material elastic and viscous moduli. In this work, we assess the validity of quantitative VisR (QVisR) in simulated materials, propose a method of domain adaption to phantom VisR displacements, and show in vivo estimates from a clinically acquired dataset.



*Index Terms*— Acoustic radiation force (ARF), elastography, machine learning, quantitative, radiomics, ultrasound, viscoelastic response (VisR), viscoelasticity.

# I. INTRODUCTION

ISSUE characterization is studied to identify measurable properties that can be correlated to clinical outcomes [1]. Considerable efforts has been spent developing quantitative, as opposed to qualitative and semiquantitative, metrics of characterization because they are better suited for cross-sectional and longitudinal clinical studies [2], [3].

Manuscript received 11 March 2024; accepted 17 May 2024. Date of publication 23 May 2024; date of current version 15 July 2024. This work was supported in part by the National Cancer Institute (NCI) under Grant R01CA275139; in part by the National Heart, Lung, and Blood Institute (NHLBI) R01HL092944; in part by the National Institute of Diabetes and Digestive Kidney Diseases (NIDDK) under Grant R01DK107740; and in part by the National Institute of Neurological Disorders and Stroke (NINDS) under Grant R01NS074057. (Corresponding author: Joseph B. Richardson.)

This work involved human subjects or animals in its research. Approval of all ethical and experimental procedures and protocols was granted by the Institutional Review Board at the University of North Carolina at Chapel Hill under Protocol No. 11-1509.

Joseph B. Richardson is with the Department of Electrical and Computer Engineering, North Carolina State University, Raleigh, NC 27695 USA (e-mail: joeyr@unc.edu).

Christopher J. Moore is with Revvity (Formerly PerkinElmer), Waltham, MA 02451 USA (e-mail: Christorpher.Moore2@revvity.com). Caterina M. Gallippi is with the Joint Department of Biomedical Engi-

neering, The University of North Carolina at Chapel Hill, Chapel Hill, NC 27514 USA (e-mail: cmgallip@email.unc.edu).

Digital Object Identifier 10.1109/TUFFC.2024.3404457

Tissue viscoelasticity is a quantitative parameter with an intuitive link to clinical outcomes since many pathologies present measurable changes in mechanical property (e.g., fibrosis and inflammation) [4], [5], [6].

The subfield of ultrasound elastography attempts to measure changes in tissue viscoelasticity. The majority of elastography methods involve tracking the physical displacement of speckle-generating scatterers constituting the interrogated tissue. The magnitude and/or rate of displacement is then associated with mechanical property through model-based or data driven approaches [7], [8]. Physical displacement of tissue is generated through external indentation or vibration, passive stresses such as breathing, or application of acoustic radiation force (ARF). Reduction to clinical practice can be challenging for techniques that use external indentation or vibration due to the need for extra equipment and/or nonstandardized application of stress [9]. Passive stress methods generally require boundary condition measurements or mathematical models that are often unknown for in vivo imaging contexts [10].

Most elastography techniques using ARF pushes track shear wave propagation OFF-axis laterally of the applied ARF push. These methods typically relate shear wave measurements (phase or group velocity and dispersion) to tissue mechanical property [7], [11], [12], [13]. Shear wave-based methods generally assume mechanical property homogeneity over the wave

#### **Highlights**

- QVisR uses a neural network trained on simulations to estimate the elastic and viscous moduli of materials given
  the displacement profile measured in the region of acoustic radiation force excitation.
- QVisR has low elastic and viscous moduli estimation RMSE in mechanically homogeneous and heterogeneous simulations and can be fine-tuned to estimate using displacements acquired with a real scanner.
- QVisR estimates both the elastic and viscous moduli without monitoring shear-wave propagation and shows promise for clinical application with improvements in model calibration.

propagation region. This assumption reduces the resolution of shear wave-based methods compared to ON-axis methods and can result in spatial averaging of mechanical property estimation if heterogeneities exist. Shear waves are also prone to reflection off out-of-plane targets, such as bone or connective tissue, which can distort the measured wave properties. Additionally, shear wave-based methods are depth limited since the ARF pushes need to generate enough displacement to support shear wave propagation over a measurable distance [7], [11].

Our lab developed viscoelastic response (VisR) ultrasound to evaluate the viscoelastic properties of tissue by approximating a creep response [14]. VisR uses a colocalized, double-push ARF excitation to minimize acquisition time when compared with similar methods (kinetic acoustic vitroretinal examination (KAVE) [15] and monitored state-state excitation and recovery (MSSER) [16]). Additionally, VisR tracks the induced displacements ON-axis with the ARF excitations to avoid the aforementioned challenges of methods that monitor shear-wave propagation. VisR displacements can be fit to a 1-D mass-spring-damper (MSD) model with fit parameters rearranged to derive semiquantitative measures of elasticity and viscosity (RE = Relative Elasticity and RV = Relative Viscosity) [17] relative to the applied force amplitude, which can be assumed constant over a small, local region [11], [18]. Additional corrections have been studied to improve comparisons of RE and RV over a wider region of interest (ROI) in an image [19], [20], [21]; however, all VisR sequence derived viscoelasticity measures have been semiquantitative.

Model-based elastography approaches become more ill-posed when a model parameter or boundary condition is unknown/immeasurable, such as the applied force amplitude for VisR. Data-driven statistical approaches, such as neural networks, often require large sets of labeled data for training that, ideally, represent all data variations present in the final test application of the network. Although experimental and clinical elastography datasets are usually small, large simulation datasets can be generated to capture variations in displacement profiles due to imaging configuration (focal depth and transducer parameters) and tissue property (viscoelasticity and attenuation).

In this study, we regress multilayer perceptron neural networks on simulated, ultrasonically tracked VisR displacement time series to jointly estimate elastic and viscous moduli. The predicted moduli are direct estimates of the underlying mechanical properties coining the term quantitative VisR (QVisR) ultrasound. This work is an extension of methods, results, and discussion presented

in [22], [23], and [24]. In [22], we evaluated bagged trees regressors models against neural network architectures on mechanically homogeneous simulations without noise and concluded that neural networks provide lower test set error. In [23], we varied the added noise levels in homogeneous materials to test QVisR performance degradation. In [24], we trained QVisR on both homogeneous and heterogeneous simulations with noise and evaluated QVisR generalizability by estimating the elasticity scans acquired in a CIRS elastic tissue-mimicking phantom. This manuscript includes extended analysis of QVisR results in homogeneous and heterogeneous simulations with noise, provides metrics related to model evaluation in CIRS phantom, and shows both simulation-trained and phantom fine-tuned QVisR estimates in the muscles of boys with Duchenne muscular dystrophy (DMD) not present in any previous work. We also provide comparisons of QVisR with conventional VisR RE and RV semiquantitative images in the phantom and clinical examples to show the benefits of quantitative viscoelasticity estimation.

#### II. METHODS

#### A. Simulations

Mechanically homogeneous and heterogeneous viscoelastic materials interrogated through a VisR beam sequence were simulated using methods adapted from the work of Palmeri et al. [25]. Fixed ARF excitation and tracking parameters across all simulations are listed in Table I. Major material and finite element parameters shared by all simulations and unique to the homogeneous and heterogeneous simulations are shown in Table II. For each set of simulations, ON-axis displacement through time data was paired with the respective axial depth, focal depth, elasticity, and viscosity of the simulation and then saved for further processing. Viscoelastic material properties were chosen to represent realistic ranges found in soft tissues [4], [5] for all simulations.

1) Homogeneous Dataset: A Siemens VF7-3 transducer (Siemens Healthineers, Issaquah, WA) was parameterized to be modeled with Field II [26]. Transducer point spread functions (PSFs) for ARF excitations and tracks were modeled using the beam sequence parameters in Table I and material properties in Table II. ARF excitation PSFs were calculated for each of the 11 focal depths enumerated in Table II.

A rectangular finite element mesh was defined using LS-DYNA (Ansys Inc., Canonsburg, PA) with 280 440 elements of volume 250  $\mu$ m<sup>3</sup> spanning a 1 × 1 × 4 cm (lateral × elevation × axial) region with axial quarter symmetry. Simulated ARF PSF intensities were converted to body forces and

TABLE I

ARF EXCITATION AND TRACKING PARAMETERS FOR SIMULATIONS AND
PHANTOM ACQUISITIONS

Name	Value				
Beam Sequence Parameters					
Transducer	VF7-3				
Elevational Lens Focus (mm)	37.5				
Sampling Frequency (MHz)	40				
ARF Center Frequency (MHz)	4.21				
ARF Duration (µs, cycles)	70, 300				
ARF F/#	3.0				
Tracking Center Frequency (MHz)	6.15				
Tracking Tx F/#	3.0				
Tracking Rx F/#*	0.75				
Tracking Tx Focus (mm)	20				
Tracking PRF (kHz)	10				
Normalized Cross Correlation Parameters					
Kernel Length (wavelengths, µm)	3, 751				
Search Window (µm)	50				

<sup>\*</sup> Aperture growth and dynamic Rx focusing enabled

TABLE II
SIMULATION PARAMETERS

Name	Value		
All Simulati	ons		
Material Model	Kelvin-Maxwell		
Poisson's Ratio 0.499			
Speed of Sound (m/s)	1540		
Acoustic Attenuation (dB/cm/MHz)	1.0		
Density (kg/m <sup>3</sup> )	1.0		
Homogeneous Simu	lations Only		
Elasticity (kPa)	5-100 step 10.56		
Viscosity (Pa.s)	0.01-7.01 step 0.78		
Focal Depth (mm)	15, 17, 20, 23, 25, 27, 30, 32, 35, 38, 40		
Heterogeneous Simu	lations Only		
Inclusion Elasticity (kPa)	15.56, 22, 28, 36.67		
Inclusion Viscosity (Pa.s)	0.01, 1.57, 2.6, 3.9		
Background Elasticity (kPa)	26.11		
Background Viscosity (Pa.s)	2.34		
Focal Depth (mm)	15-35 step 5		
Inclusion Diameter (mm)	10		
Inclusion Depth (mm)	25		
Inclusion Lateral Offset (mm)	0, 2.5, 4, 7		

mapped to nodes on the mesh. LS-DYNA material files were created on a grid of ten elasticities (5–100 kPa in 10.56-kPa steps) and ten viscosities (0.01–7.01 Pa.s in 0.78-Pa.s steps) for a total of 100 material combinations. Each material was defined with the Kelvin–Maxwell Viscoelastic material model, a Poisson's Ratio of 0.499, and an equivalent elastic perfectly matched layer (PML). Finite element simulations were performed for every material combination and focal depth. Each

simulation applied nodal forces with a VisR beam sequence and evaluated the resulting nodal displacements through time by solving the dynamic equations of motion between nodes. The simulations were carried out over 4.36 ms with a control time step of 1  $\mu$ s, a sampling period of 25  $\mu$ s, and two successive 70  $\mu$ s (300 cycle) ARF pushes applied at 5 and 442  $\mu$ s, respectively. Finite element hourglassing control type (ihq) of 4 and hourglassing coefficient (qh) of 0.10 were set for all elements in the mesh.

Nodal displacements for each time step were translated to scatterer displacements in five uniform scattering phantoms with randomly generated initial scatterer positions and 11 scatterers per resolution cell. Scatterers were tracked in Field II with the previously generated track PSFs in each phantom with a pulse repetition frequency (PRF) of 10 kHz. White Gaussian noise from 30- to 50-dB signal-to-noise ratio (SNR) was added in steps of 10 dB to the received RF data before scatterer displacement was estimated with 1-D axial normalized cross correlation ( $3\lambda$  kernel, 50- $\mu$ m search window) [27] generating 1559 displacement through time profiles from 10 to 40 mm axially. Each displacement profile was treated as an independent sample resulting in 34 298 000 simulated displacement profiles (focal depths × elasticities × viscosities × scatterer realizations × SNRs × axial depths).

2) Heterogeneous Dataset: Heterogeneous simulations were carried out in a similar manner to the homogeneous simulations aside from the focal depths and material properties. Beginning with the finite element mesh formed for the homogeneous simulations, a 10-mm diameter spherical inclusion was placed with centroid at an axial depth of 25 mm. LS-DYNA material files were generated on a grid of four inclusion elasticities (15.56, 22, 28, and 36.67 kPa), four inclusion viscosities (0.01, 1.57, 2.6, and 3.9 Pa.s), and a single background viscoelasticity (26.11-kPa elasticity, 2.34-Pa.s viscosity). The background viscoelasticity was selected to match a set of homogeneous simulations, and the inclusion viscoelasticities were varied around the background values to provide both lower and higher contrast sets of simulations. The ARF excitation PSFs were calculated at five focal depths (15–35 mm in 5-mm steps) to interrogate the medium above, below, within, and at the boundary of the inclusion. Additionally, ARF excitations were applied at four lateral offsets from the center of the inclusion (0, 2.5, 4, and 7 mm) to model the effects of pushing closer to the lateral inclusion boundary and, in the extreme case of a 7-mm lateral offset, pushing outside of the inclusion. In total, the heterogeneous dataset consisted of 9 977 600 simulated displacement profiles (focal depths × inclusion elasticities × inclusion viscosities × scatterer realizations  $\times$  SNRs  $\times$  axial depths  $\times$  lateral offsets).

#### B. Scanner Acquisitions

1) Phantom Acquisitions: Imaging of a CIRS Cylindrical Elasticity QA Phantom (CIRS, Norfolk, VA) was performed with a Siemens Acuson Antares scanner and a VF7-3 linear array transducer (Siemens Healthineers, Issaquah, WA). Custom VisR beam sequences were created through the Axius Direct Ultrasound Research Interface (URI) allowing access to the raw radio frequency data. The imaging sequence executed

a raster scan focused B-Mode acquisition followed by a VisR sequence at each of 40 lateral locations evenly spaced over 20 mm for 2-D VisR imaging. The VisR sequences used the beam sequence parameters listed in Table I and consisted of two reference tracks, two ARF excitations, four tracks between the ARF excitations, and 40 tracks after the second ARF excitation.

The imaging sequence was applied to the transverse cross section of the 30-mm-deep cylindrical inclusions forming 2-D images with circular inclusions. Data were acquired for each inclusion type (four inclusion elasticities) and the largest three circular cross-section diameters (6.49, 10.41, and 16.67 mm) at three focal depths (25, 30, and 35 mm). Each acquisition was repeated twice; however, only the first acquisition was used unless an error occurred in the data collection routine. True elastic modulus measurements calibrated by CIRS were reported as follows: Background (26 kPa), Type 1 Inclusion (6.5 kPa), Type 2 Inclusion (15.3 kPa), Type 3 Inclusion (49 kPa), and Type 4 Inclusion (88 kPa).

2) Clinical Acquisitions: Samples from a previously acquired clinical dataset were processed similar to those from the CIRS phantom. The clinical data set included VisR data acquired in the lower limb muscles of male patients, aged 5–10 years, with DMD and in age-match control boys with no known neuromuscular disorders. Data acquisitions were performed using the same scanner, transducer, and sequencing as listed in the phantom acquisitions section. All acquisition procedures were approved by the Institutional Review Board (IRB) of the University of North Carolina at Chapel Hill. Further information on the collection and composition of this dataset are reported in [28].

3) Scanner Processing: Raw acquisition data from the scanners was transferred to workstations for custom processing. B-mode images were created through the absolute value of the log-compressed, Hilbert-transformed RF data. VisR displacements were estimated with 1-D axial normalized cross correlation with parameters listed in Table I. A linear motion filter was applied to each displacement to remove any low-frequency bulk displacements from the acquisition process [29]. For each phantom acquisition, ON-axis displacement through time data were paired with the respective axial depth, focal depth, calibrated elasticity, and assumed viscosity and saved for use in model fitting. Clinical acquisitions were similarly saved aside from pairing with the true elasticity and viscosity, which is unknown. The clinical acquisition system SNR is estimated to be roughly 40 dB given that the muscle tissue were echogenic, stationary through the acquisition cycle, and did not contain any large structures with blood flow.

# C. Semiquantitative Viscoelastic Response Model Fit Procedure

Ultrasonically tracked VisR displacements are fit to an MSD second-order nonhomogeneous differential equation [17], [21]. The MSD model is equivalent to a Kelvin-Voigt viscoelastic model with the addition of an acceleration term with mass coefficient which captures some of the complex inertial effects of tissue deformation induced by transient ARF pushes. The

base form of the MSD model is as follows:

$$m\ddot{z}(t) + \eta \dot{z}(t) + \mu z(t) = Au(t) \tag{1}$$

where m [Kg] is the mass,  $\eta$  [Nm<sup>-1</sup>s] is the damper viscosity,  $\mu$  [Nm<sup>-1</sup>] is the spring stiffness, A[N] is the applied force magnitude, z(t) [m] is the time-dependent axial displacement, and u(t) is the time-dependent applied VisR force profile. The VisR force profile can be modeled as a series of time-delayed ARF pushes through the following equation:

$$u(t, t_{ARF}, t_s) = H(t) - H(t - t_{ARF}) + H(t - t_{ARF} - t_s) - H(t - 2t_{ARF} - t_s)$$
(2)

where H denotes a heavyside step function,  $t_{ARF}[s]$  is the ARF push duration, and  $t_s[s]$  is the time between the two ARF pushes. This equation generates two square impulses that approximate the applied forcing function of a double-push VisR beam sequence. Combining (1) and (2) and rearranging coefficients leads to the following form:

$$\ddot{z}(t) + \omega^2 \tau \dot{z}(t) + \omega^2 z(t) 
= S\omega^2 [H(t) - H(t - t_{ARF}) + H(t - t_{ARF} - t_s) 
- H(t - 2t_{ARF} - t_s)]$$
(3)

where  $\omega$  [s<sup>-1</sup>] is the natural frequency,  $\tau$  [s] is the material relaxation time constant, and S [m] is the system static sensitivity. These coefficients are defined as follows:

$$\omega = \sqrt{\frac{\mu}{m}}, \quad \tau = \frac{\eta}{\mu}, \quad S = \frac{A}{\mu}.$$
 (4)

An analytic expression for z(t) in (3) is found in the Laplace domain. Nonlinear optimization (Nelder–Mead algorithm) is then used to estimate the coefficients ( $\omega$ ,  $\tau$ , and S) that minimize the difference between the analytic displacement z(t) and ultrasonically tracked displacement measurements. Once the fit procedure is complete, the coefficients are rearranged into the semiquantitative estimates of elasticity and viscosity, RE [m<sup>-1</sup>] and RV [m<sup>-1</sup>s], respectively,

$$RE = \frac{1}{S} = \frac{\mu}{A}, \quad RV = \frac{\tau}{S} = \frac{\eta}{A}.$$
 (5)

These parameters are considered semiquantitative measures of elasticity and viscosity because each is estimated relative to the unknown applied force amplitude, A. Considering A varies over axial depth due to the focusing effects of the applied ARF push PSF, a depth-compensation factor is applied to RE and RV. Additionally, since fitting displacements to a series of 1-D MSD models does not capture the complex system inertia that develops in an actual tissue environment, a simulation-derived elasticity compensation factor is applied to the RV estimates. Briefly, in a continuum environment, the displacement recovery measured ON-axis to the ARF push is due to both the viscoelastic recovery effects of the media as well as the spatially averaged measure of viscoelastic shearing effect [30]. The shearing effect is measured as an artificially prolonged displacement recovery, which results in an overestimation of viscosity when using the 1-D MSD model. Further details for the derivation and application of the depth and elasticity compensation factors are documented in [21].

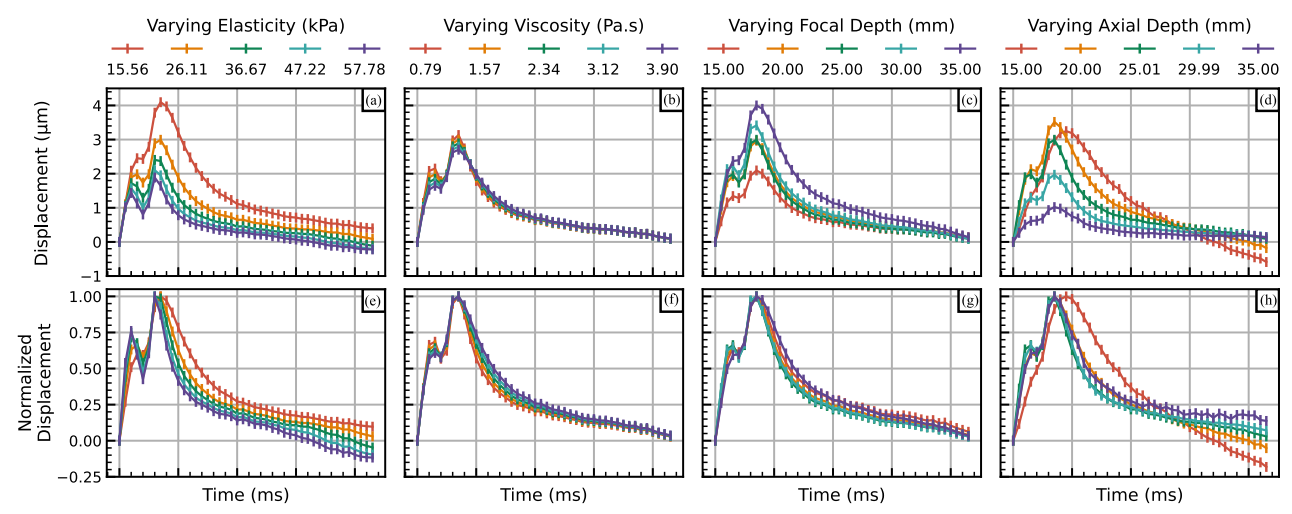


Fig. 1. Simulated VisR displacement profiles before (top row) and after (bottom row) max normalization as (a) and (e) elasticity, (b) and (f) viscosity, (c) and (g) focal depth, and (d) and (h) axial depth vary. When not varying, the following fixed parameters were used: elasticity = 36.67 kPa, viscosity = 2.34 Pa.s, focal depth = 25 mm, axial depth = 25 mm, and SNR = 40 dB. Note that the green displacements in each subplot have equivalent parameters.

# D. Quantitative Viscoelastic Response Machine Learning Model Training and Evaluation

1) Preprocessing: Max normalization was applied to each displacement profile to remove amplitude differences caused primarily by the unknown applied force distribution (see Fig. 1). Min-max normalization over the respective global parameter range was used for axial depth, focal depth, elasticity, and viscosity to homogenize the data scales from 0 to 1. The focal depth variable refers to the ARF push focus and the axial depth is the displacement estimation kernel location. Displacements were concatenated with the associated axial depth and focal depth of each profile to create the model inputs, and elasticity and viscosity were grouped as the outputs. Dataset generation for each acquisition type is described in greater detail below:

Simulation datasets were grouped into homogeneous simulations only (Train<sub>Hom</sub>, Test<sub>Hom</sub>), heterogeneous simulations only (TrainHet, TestHet), and a mixture of the two (Train<sub>Mix</sub>, Test<sub>Mix</sub>). The primary difference between the training/validation and testing sets for simulations was the random scatterer realization since this variable would model noisy differences in the posterior distribution of the viscoelasticity estimates. Samples from each dataset were assigned a draw probability to balance classes during training. For example, the background samples of the TrainHet dataset were assigned a lower draw probability than the inclusion samples because the background for all heterogeneous simulations was the same viscoelastic material combination, whereas the inclusion material combinations varied. Validation sets were generated as 350 000 sample random splits from the training sets using the aforementioned draw probabilities. To account for different training set sizes for the Train<sub>Hom</sub>, Train<sub>Het</sub>, and Train<sub>Mix</sub> datasets, an epoch was defined as a random weighted draw of 2 million total samples, e.g., an epoch of Train<sub>Hom</sub> draws 2 million homogeneous samples and an epoch of Train<sub>Mix</sub> draws 1 million homogeneous samples and 1 million heterogeneous samples.

Phantom images were cropped axially to only include data between 22 and 38 mm to reduce oversampling of the single background elasticity. Phantom displacements were linearly interpolated to match the simulation time grid so that model inputs were the same length (43 samples).

2) Model Selection: A Bayesian hyperparameter search was executed for each of the training datasets to minimize the combined Huber loss of the elasticity and viscosity estimates on the validation sets [31]. Huber loss acts as L2, or Mean Square Error, loss within a delta range and L1, or Mean Absolute Error, outside of this range, providing regularization. Given the elasticities and viscosities were min-max normalized between 0 and 1, the delta range was set to 1, so the Huber loss acted as L2 when the summed estimate errors were within normalization ranges and L1 otherwise. Additionally, combining losses with this normalization equally weights penalties for elasticity and viscosity estimates. This search found similar optimal hyperparameters for each training dataset, and so the Train<sub>Mix</sub> parameters were used for all cross-validation runs to standardize training. Using the random weighted sampling procedure described above, 11 cross-validation runs were performed for each train dataset resulting in 33 trained models.

For each cross-validation training run, a fully connected, feed-forward, multilayer perceptron neural network model was trained for 150 epochs with an ADAM optimizer [32], a learning rate  $\lambda$  of 0.0037, first moment  $\beta_1$  of 0.9, second moment  $\beta_2$  of 0.999, a batch size of 4096 samples, and early stopping. The model consisted of four hidden layers with the following neuron count connecting each layer: 128, 256, 256, 128, and 64. The concatenated displacements, axial depth, and focal depth had an input size of 45, and jointly estimating elasticity and viscosity gives an output size of 2. Hidden layer neurons used Tanh activation functions and Softplus activation was used on the two output neurons to constrain the model to positive elastic and viscous moduli predictions. Model performance results are reported as the root mean square error (RMSE).

3) Fine-Tuning: Using model weights trained with simulated data, fine-tuning was performed by lowering the learning rate to 0.0001 and further training for five epochs on the phantom displacements. Early stopping was employed while

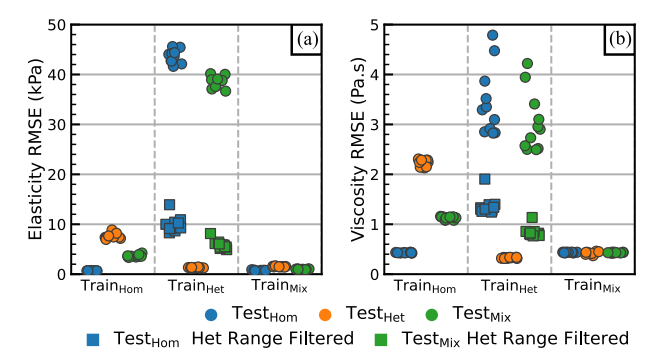


Fig. 2. (a) Elasticity and (b) viscosity RMSE grouped by train and test simulation datasets for each cross-validation training run. RMSEs displayed are over samples in the test sets (color) with an SNR of 50 dB. Square marker points represent the subset of Test<sub>Hom</sub> and Test<sub>Mix</sub> with parameter ranges filtered to match Train<sub>Het</sub> ranges (e.g., Test<sub>Hom</sub> elasticities greater than 36.67 kPa were removed since 36.67 kPa is the max elasticity in Train<sub>Het</sub>).

monitoring the combined Huber loss on simulation and phantom displacement estimates on the validation sets. The fine-tuning training set contained phantom acquisitions from the 10.41- and 16.67-mm cross-sectional diameter inclusions with 25- and 35-mm focal depths. Performance was tested on the 6.49-mm cross-sectional diameter inclusion with a 30-mm focal depth.

#### E. Performance Metrics

Quantitative elasticity and viscosity estimations using QVisR are evaluated with the quantitative RMSE metric [33]. Given the large sample sizes and approximately normal error distributions, RMSE is appropriate to give an average estimate of the error in the correct unit of the estimate (kPa for elasticity and Pa.s for viscosity). When comparing semiquantitative estimates of elasticity and viscosity (VisR RE and RV) to each other and to the quantitative estimates, the semiquantitative metric, generalized contrast to noise ratio (gCNR), is used [34]. This metric allows comparison of the ability to delineate the contrast between image patches independently of any dynamic range transformations to the data.

#### III. RESULTS

Fig. 2(a) and (b) shows QVisR elasticity and viscosity estimation RMSE for each train and test material subset pairing cross-validation run. Neural networks are poor at extrapolation [35], so results for the Train<sub>Het</sub> models were filtered to exclude estimates on Test<sub>Hom</sub> samples that were outside of the simulated heterogeneous dataset parameter ranges (filtered subset RMSEs represented by square markers in Fig. 2).

Fig. 3 depicts QVisR Train $_{\rm Mix}$  model RMSEs on the Test $_{\rm Hom}$  dataset grouped by axial distance to the focal depth. Due to displacement profiles being measured only from 10 to 40 mm, some focal depths within the distance to focal depth ranges (colors) have sparse data as illustrated by truncated lines in Fig. 3(c) and (f). Results are shown with varying test set elasticity, viscosity, and focal depth.

Fig. 4 compares QVisR Train<sub>Mix</sub> model RMSEs on the Test<sub>Mix</sub> set when grouped by SNR. Results are shown with varying test set elasticity, viscosity, focal depth, and scatterer

TABLE III
CIRS PHANTOM GCNR VALUES FOR VARYING ROI PATCH SIZES

Parameter	ROI Size	Inc. Type 1	Inc. Type 2	Inc. Type 3	Inc. Type 4
VisR MSD Relative Elasticity	2 x 2 mm	0.79	0.93	0.29	0.92
	3 x 3 mm	0.69	0.95	0.36	0.69
	4 x 4 mm	0.70	0.73	0.28	0.77
Simulation Trained QVisR Elasticity	2 x 2 mm	1.00	0.95	0.98	0.40
	3 x 3 mm	1.00	0.97	0.95	0.55
	4 x 4 mm	0.97	0.90	0.78	0.55
Phantom Fine Tuned QVisR Elasticity	2 x 2 mm	1.00	1.00	1.00	1.00
	3 x 3 mm	1.00	1.00	1.00	1.00
	4 x 4 mm	1.00	0.97	0.98	1.00

realization. At 20-dB system SNR, the estimate RMSEs are no longer viable representing a lower limit of noise where QVisR is no longer a good estimator. Significant spiked decreases in RMSE for lower SNRs (≤30 dB) at elastic moduli of 22 and 28 kPa as well as viscous modulus of 2.34 Pa.s indicate moduli that are present only in the heterogeneous dataset. Similar alternating spikes in the focal depth subplots are also caused by these moduli since the RMSE at each focal depth is averaging over all elasticities and viscosities and the lower RMSE spikes occur at the focal depths in the heterogeneous dataset.

Fig. 5 shows the point-wise axial QVisR estimates of elasticity and viscosity in heterogeneous inclusion simulations. Results are shown for heterogeneous materials with the following inclusion elastic and viscous moduli pairs: (15.56 kPa, 0.01 Pa.s), (15.56 kPa, 3.90 Pa.s), (36.66 kPa, 0.01 Pa.s), and (36.66 kPa, 3.90 Pa.s). The heterogeneous material background was held constant with 26.11-kPa elastic modulus and 2.34-Pa.s viscous modulus. Heterogeneous material axial estimation results are shown at four lateral offsets from the inclusion center (0, 2.5, 4.0, and 7.0 mm). The 7.0-mm lateral offset measurements are completely outside the inclusion boundary so the material is homogeneous over the axial extent [see Fig. 5(d) and (i)]. Results in a separate homogeneous simulation matching the heterogeneous simulation background viscoelasticity are also plotted [see Fig. 5(e) and (j)].

Fig. 6 shows the VisR MSD RE as well as both simulation-trained and phantom fine-tuned QVisR elasticity estimation results in the CIRS cylindrical elasticity phantom test set. True elasticity masks created from manual B-Mode segmentation illustrate the target elasticity for each model [see Fig. 6(a)–(d)]. Model results are shown for each of the four calibrated inclusion elasticities (6.5, 15.3, 49.0, and 88.0 kPa). Overlaid on the figure are semiquantitative (gCNR) and quantitative (RMSE) metrics with corresponding ROI patch sizes of 2 × 2 mm. The gCNR metric uses a patch within the center of the inclusion and one to the right of the inclusion while RMSE is measured per patch. Table III lists the changes in the gCNR metric as the image patch size increases to encompass most of the interior of the inclusion and more of the boundary pixels.

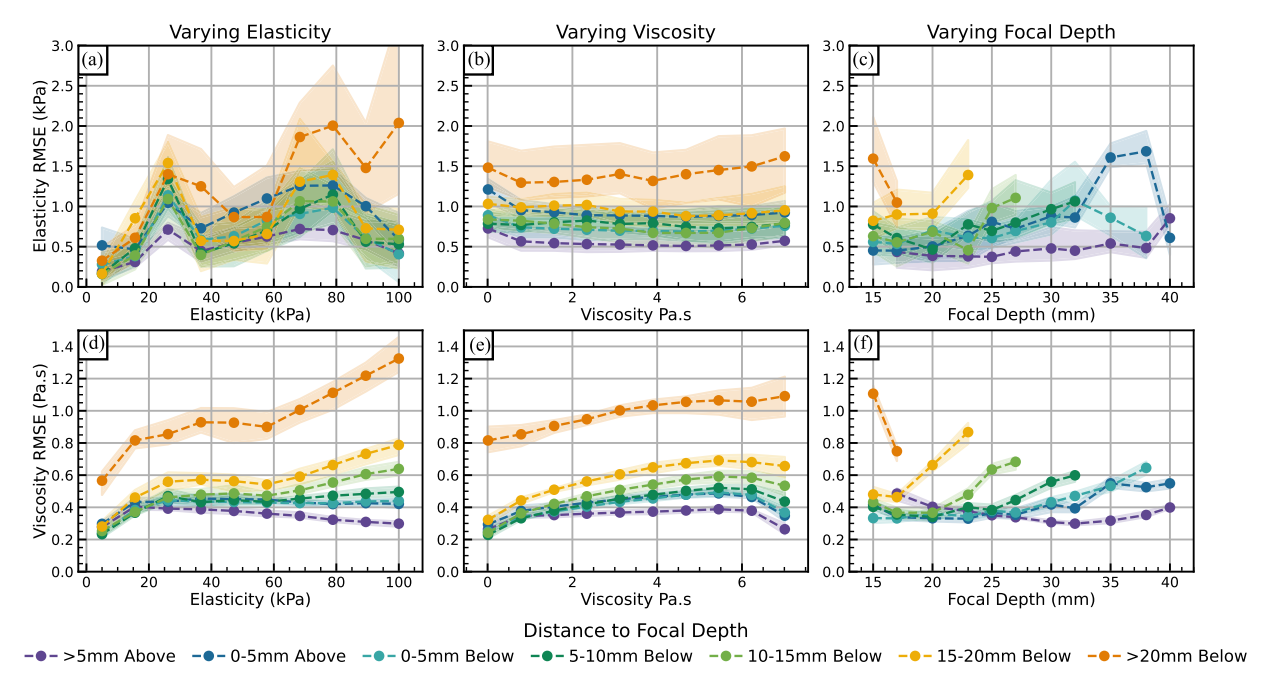


Fig. 3. Elasticity [top row, (a)–(c)] and viscosity [bottom row, (d)–(f)] RMSE grouped by distance from displacement axial depth to ARF push focal depth with varying elasticity [left column, (a) and (d)], viscosity [middle column, (b) and (c)], and focal depth [right column, (c) and (f)]. Points and shading represent the mean  $\pm$  max and min RMSE over the 11 cross-validation Train<sub>Mix</sub> models. RMSEs were calculated over all seed realizations with an SNR of 50 dB in the Test<sub>Hom</sub> dataset.

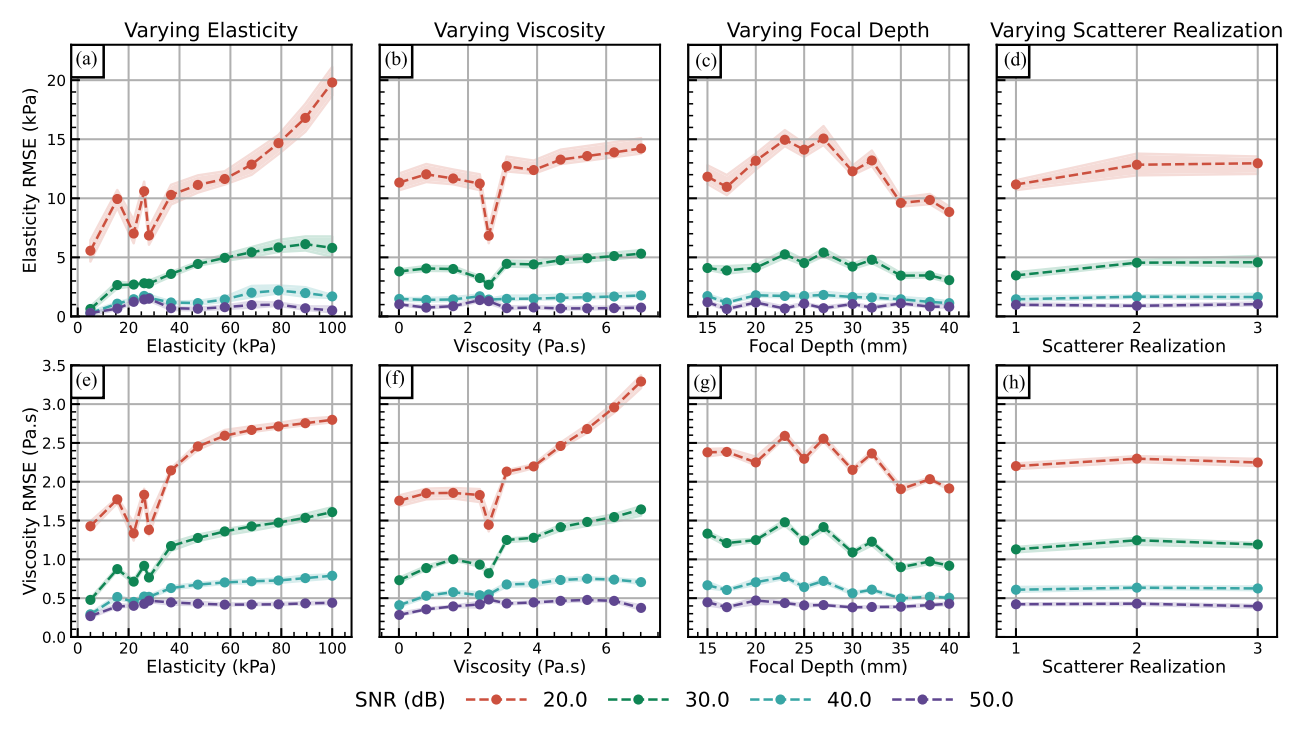


Fig. 4. Elasticity [top row, (a)–(d)] and viscosity [bottom row, (e)–(h)] RMSE grouped by SNR for varying elasticity [first column, (a) and (e)], viscosity [second column, (b) and (f)], focal depth [third column, (c) and (g)], and scatterer realization [fourth column, (d) and (h)]. Points and shading represent the mean  $\pm$  max and min RMSE over the 11 cross-validation Train<sub>Mix</sub> models. RMSEs calculated over all samples in the Test<sub>Mix</sub> set except those greater than 20 mm below the focus.

Fig. 7 shows B-Mode, peak displacement, VisR MSD RE and RV, and both simulation-trained and phantom fine-tuned QVisR viscoelasticity estimates in the gastrocnemius and rectus femoris muscles of two boys with DMD. The simulation trained model, and base model used for fine-tuning, is the Train<sub>Mix</sub> cross-validation model with the lowest Test<sub>Mix</sub> RMSE. Displacements within key ROIs, labeled in Fig. 7, are shown in Fig. 8.

## IV. DISCUSSION

QVisR was found to work best when trained with a mixture of homogeneous and heterogeneous materials (see Fig. 2). Although the  ${\rm Train}_{\rm Mix}$  model had the lowest RMSE for the  ${\rm Test}_{\rm Mix}$  dataset, the  ${\rm Train}_{\rm Hom}$  and  ${\rm Train}_{\rm Het}$  models had slightly better performance on their, respectively, material subset test datasets than the  ${\rm Train}_{\rm Mix}$  model. Additionally, each train/test set pairing had minimal bias (<0.1 kPa, <0.03 Pa.s), and

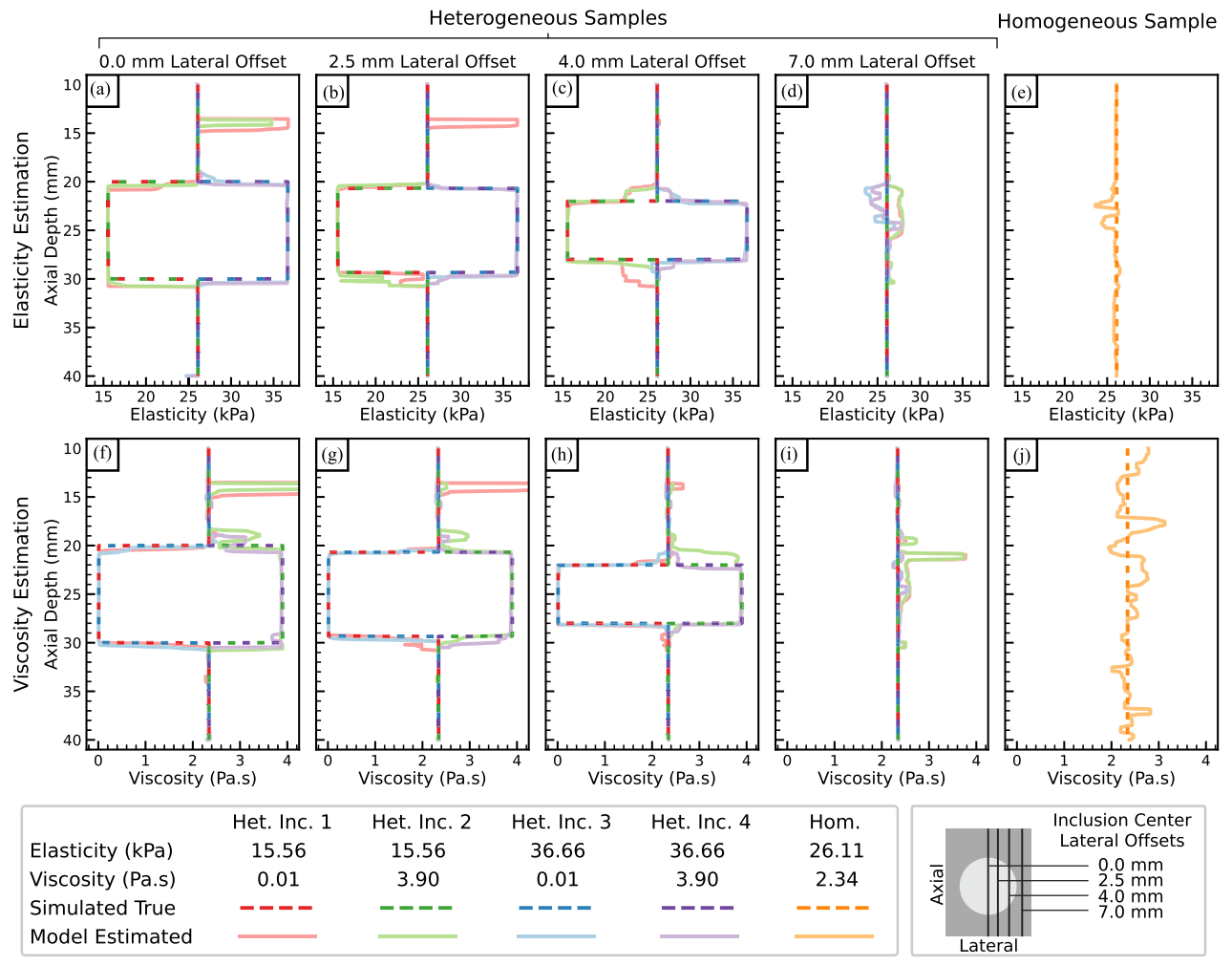


Fig. 5. Point-wise axial estimates of elasticity [top row, (a)–(e)] and viscosity [bottom row, (f)–(j)] for heterogeneous and homogeneous simulation samples. Four heterogeneous inclusion viscoelasticity combinations (colors) are shown for each inclusion center lateral offset. (a)–(d) and (f)–(i) Homogeneous sample matched the background viscoelasticity of the heterogeneous samples. (e) and (j) Estimates (solid lines) are plotted over true (dashed lines) elasticities and viscosities. Each sample was drawn from a random seed realization in the Test<sub>Mix</sub> set and have a fixed focal depth of 25 mm and 40-dB SNR. Estimate results are plotted with a  $\sim$ 1-mm sliding axial median filter. Estimates shown for the Train<sub>Mix</sub> cross-validation model with the lowest Test<sub>Mix</sub> RMSE.

errors were approximately normally distributed. RMSEs can therefore be interpreted as a standard deviation capturing 68% of the error variation, e.g., 68% of the  ${\rm Train_{Mix}}$  model elasticity estimates on the  ${\rm Test_{Mix}}$  dataset were within  $\pm 2.54$  kPa of the true elasticity. Filtering by test subset brought RMSEs down to comparable levels with  ${\rm Train_{Hom}}$  errors; however, training with both homogeneous and heterogeneous simulations still provided the best or comparable performance to models trained with each set individually. These results suggest that QVisR estimates depend on material geometry in cases where the boundary effects distort the displacement profiles. QVisR models designed to generalize to arbitrary material geometries will require training on a much greater array of simulated material geometries than presented in this study. For the remaining simulation analyses,  ${\rm Train_{Mix}}$  models are used.

When isolated to estimating on homogeneous materials to study model performance over the axial extent (see Fig. 3), QVisR elasticity and viscosity estimate RMSEs are consistent over all axial depth groups aside from greater than 20 mm below the focal depth (orange). In limited cases where the true elastic modulus is less than ~80 kPa, the elasticity estimation

RMSE is also consistent >20 mm below the focal depth [see Fig. 3(a)]. This wide axial extent of stability is thought to be due to the combination two factors. First, the relatively high acoustic attenuation coefficient of 1 dB/cm/MHz spreads the force distribution over the axial extent [11], particularly in the near field, causing several micrometer displacements far from the focus. Second, peak-normalizing each displacement profile and pairing it with both the measurement axial depth and the ARF push focal depth acts as a type of depth normalization allowing QVisR to estimate viscoelasticity far from the focus. Training QVisR models on millions of displacements with varying ARF focal depth, measurement axial depth, and material property results in a network that can compensate for complex system inertia peak displacement time delays that appear similar to an increase in viscosity. The effect of force distribution on QVisR estimates, specifically the modification of the acoustic attenuation coefficient and focal configuration, is a topic of ongoing research. For example, using a lower acoustic attenuation will make the applied force more localized and may disrupt QVisR estimates far from the focal depth. For the remaining simulation analyses, estimates greater than

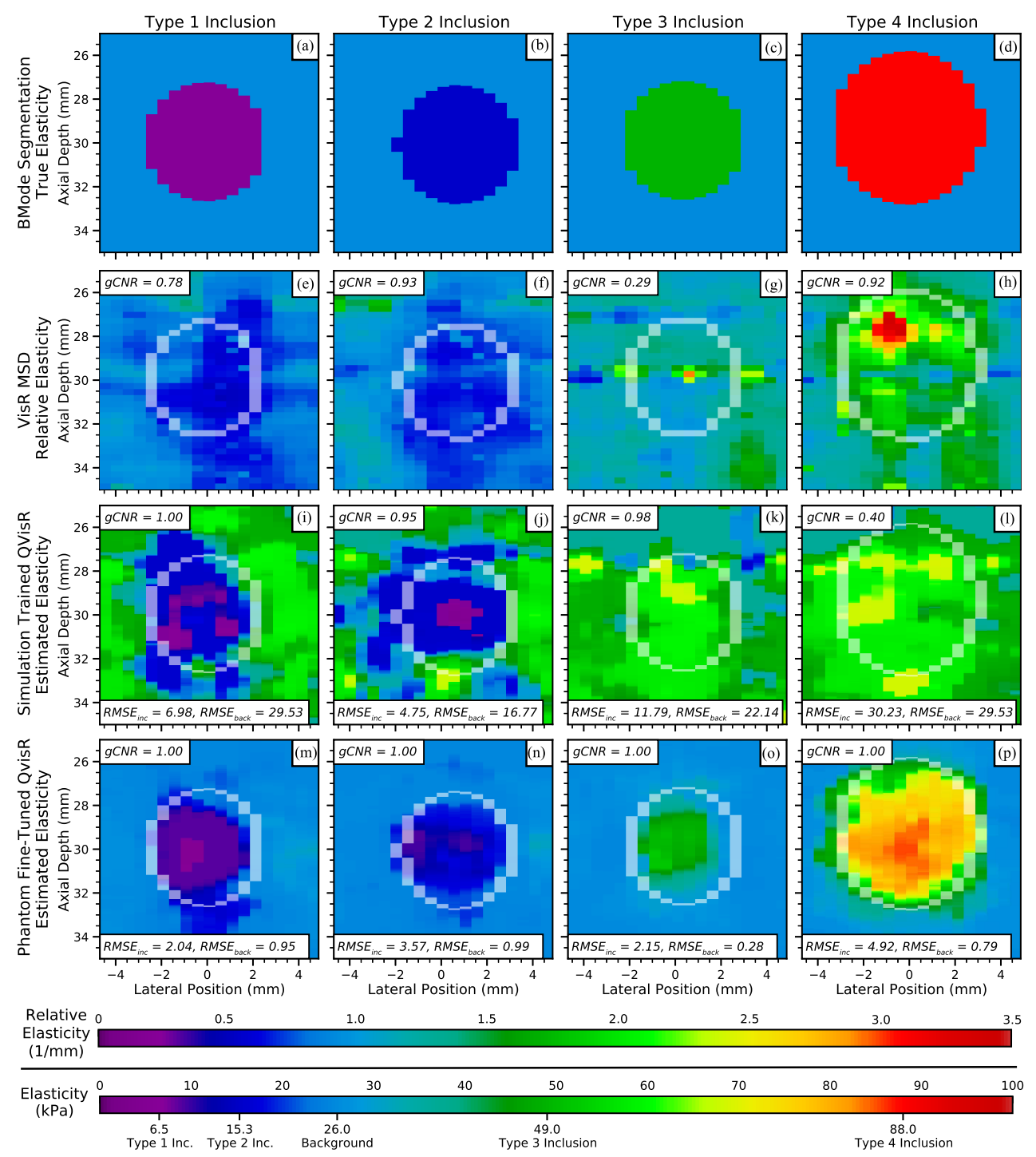


Fig. 6. Calibrated cylindrical step phantom bmode-segmented true elasticity reference [first row, (a)–(d)] compared with VisR MSD model fit RE [second row, (e)–(h)] and QVisR estimated elasticities before [third row, (i)–(l)] and after [fourth row, (m)–(p)] fine-tuning. Each column is a different inclusion type with varying inclusion elasticity and a fixed background elasticity (calibrated inclusion and background elasticities marked on the elasticity colorbar). The segmentation mask inclusion boundary is overlaid in transparent white on the estimate images to mark the outer extent of the inclusion. VisR displacement acquisitions had a 30-mm ARF push focal depth. Estimates are displayed with a 2-D median filter with a  $\sim 1 \times 0.5$  mm kernel (axial  $\times$  lateral). Overlaid statistics were calculated using 2-mm square image patches in the center of the inclusion and to the right of the inclusion. RMSE in the inclusion and background were calculated over the respective image patches with the ground truth from an equivalent size patch from the first row of images and gCNR was calculated using the inclusion and background patch of each image. Note that RMSE cannot be calculated for VisR MSD RE because RMSE is a quantitative metric and RE is a semiquantitative parameter; however, gCNR, a semiquantitative metric, can be applied to both semiquantitative and quantitative images. RMSE is in units of kPa Young's modulus.

20 mm below the focus are considered beyond the useful range of the model and excluded.

Estimates are also stable over a range of scanner realistic system SNRs (see Fig. 4). The homogeneous dataset elasticity and viscosity step sizes (10.56 kPa and 0.78 Pa.s,

respectively) were considered acceptable RMSE cutoffs when estimating across large data subsets. QVisR meets this criteria for both elasticity and viscosity RMSE across all variations of elasticity, viscosity, focal depth, and scatterer realization when the SNR is at least 40 dB; however, only elasticity

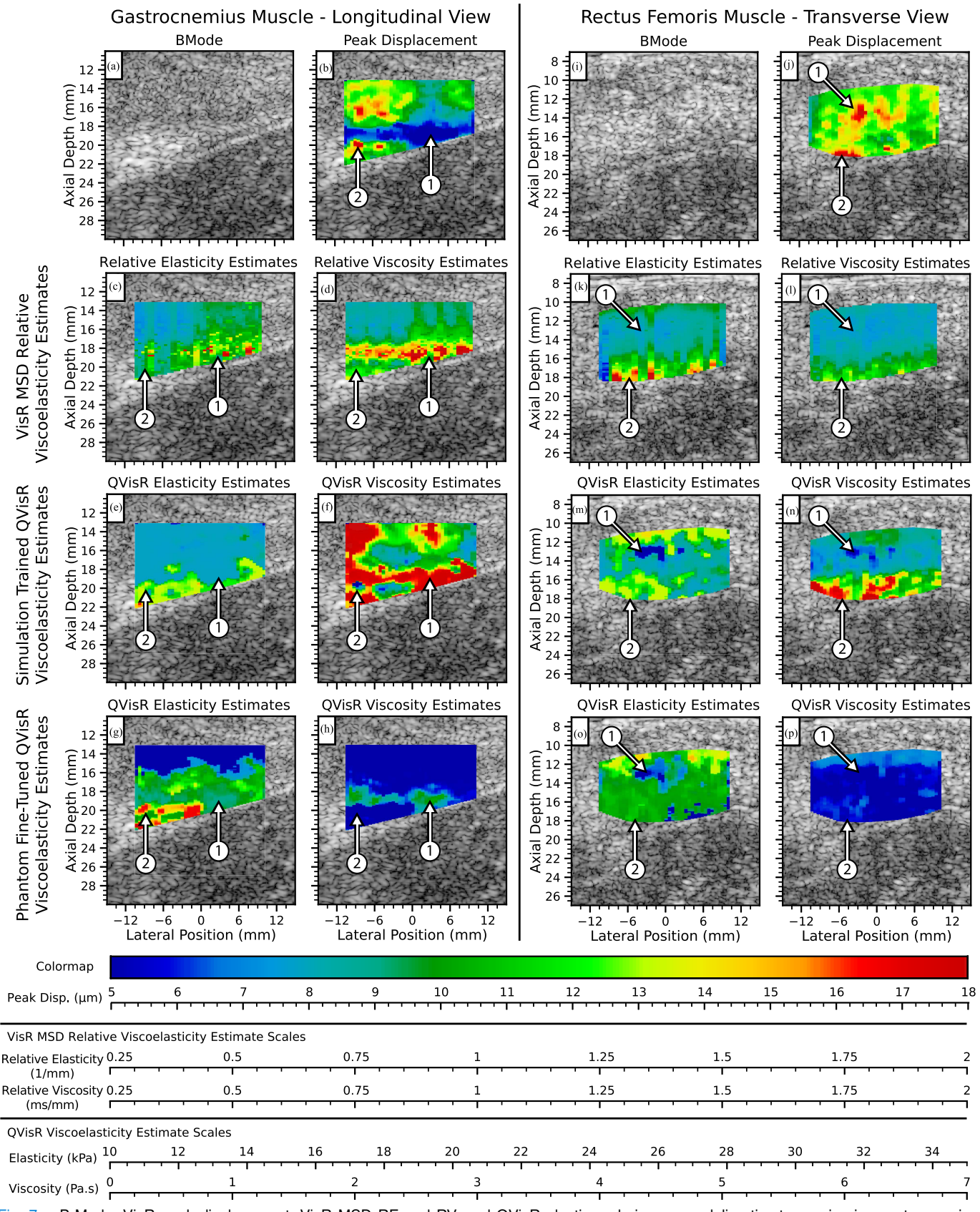


Fig. 7. B-Mode, VisR peak displacement, VisR MSD RE and RV, and QVisR elastic and viscous moduli estimates on in vivo gastrocnemius [left, (a)–(h)] and rectus femoris [right, (i)–(p)] muscles of boys with DMD. QVisR estimates are shown for the simulation trained model [third row, (e)–(f) and (m)–(n)] and the phantom fine-tuned model [fourth row, (g)–(h) and (o)–(p)]. Acquisitions had 20- (left) and 17-mm (right) ARF push focal depths and estimates are displayed with a 2-D median filter with  $\sim$ 1 × 0.5 mm kernel (axial × lateral) on the image overlays. Peak displacement images (b) and (h) were depth normalized with a parabolic curve fit to minimize variations due to applied force amplitude around the focal depth.

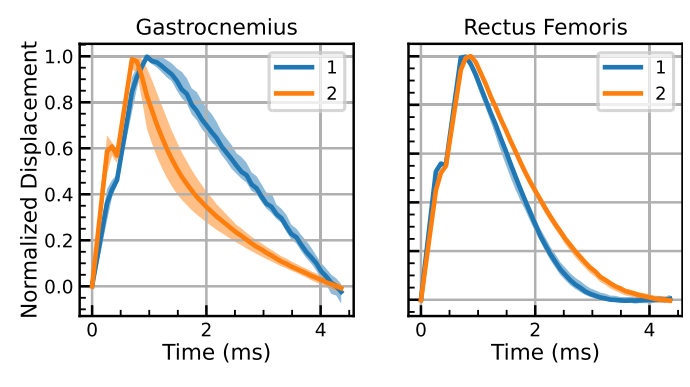


Fig. 8. VisR displacement profiles from gastrocnemius (left) and rectus femoris (right) muscle ROIs. Shading shows the min and max displacement over a 0.5-mm axial kernel. Legend labels 1 and 2 correspond to regions 1 and 2 in each Fig. 7 muscle.

RMSE is within the tolerance down to 30-dB SNR. This suggests elasticity is easier for QVisR to estimate in noisier environments than viscosity. One possible explanation for this result could be determined by visually inspecting the peak normalized displacements as elasticity and viscosity vary [see Fig. 1(e) and (f)]. Changes in displacement as viscosity varies are less dramatic than changes in displacement as elasticity varies, so it is intuitive that elasticity would be easier to estimate from the displacement profile at a lower SNR. Further analysis is necessary for proper characterization of QVisR's performance in lower SNR environments.

Shifting from evaluation of error data subset groups to individual estimate error, QVisR estimates closely match the true viscoelastic moduli through axial depth (see Fig. 5). Heterogeneous sample estimates delineate the viscoelastic inclusion boundary within 1 mm of the true boundary despite focusing at the center of the inclusion [see Fig. 5(a)–(c) and (f)-(h)]. Background viscoelasticity is estimated with negligible error aside from a large overestimate around 15 mm for samples with lower inclusion elastic modulus [see Fig. 5(a), (b), (f), and (g)]. These large overestimation errors may be caused by speckle bias, reflection artifacts off the top of the inclusion, or estimating close to the edge of simulated focal depths. When focusing with a lateral offset outside the inclusion boundary, estimate errors increase within the axial range of the inclusion projection [20–30 mm, see Fig. 5(d) and (i)]. When looking at estimates of a simulation without an inclusion and matching viscoelastic modulus to the heterogeneous sample background, a similar error profile is seen for the elastic modulus estimates but not for the viscous modulus estimates [see Fig. 5(e) and (j)], although the homogeneous viscous modulus estimates have a higher variance, which may obfuscate the viscous error profile. The repeated error profiles in both heterogeneous samples measured in the background and matched viscoelastic modulus homogeneous samples indicate a slight model bias (1–2-kPa elastic modulus, 0.5-1.0-Pa.s viscous modulus) based on the training set inclusion geometry. Additionally, the error profiles appear larger for the heterogeneous background cases implying a slight distortion of the displacement profiles due to reflections off the inclusion boundary. These insights are significant given that the model inputs are just the displacement profile, axial depth, and focal depth, so the Train<sub>Mix</sub> models have no a priori information about the existence of an inclusion or information from neighboring displacement profiles. This suggests QVisR trained on simulations with more material geometries may still accurately estimate near the inclusion boundaries.

#### A. Phantom Acquisitions

Testing QVisR generalization on CIRS calibrated elastic phantom images (see Fig. 6) shows that fine-tuning is necessary for quantitative domain adaption. Phantom image estimates for the model trained only on simulation data show the correct trends (i.e., estimates correctly identify when the inclusion is softer or stiffer than the background and generally indicate that stiffness increases with true inclusion elasticity), but the estimates have large errors and poor boundary delineation [see Fig. 6(i) and (j)]. After fine tuning [see Fig. 6(m)-(p)], QVisR both delineates the inclusion boundary and estimates the elastic moduli of the inclusion and background with a lower RMSE; however, the softest and stiffest inclusions [see Fig. 6(m) and (p)] are still under and overestimated, respectively. Elasticity estimation with QVisR somewhat gradually transitions from inclusion to background values across the inclusion boundary leading to higher RMSE near the boundary than near the center of the inclusion. Viscosity estimates are not shown since the phantom only had elasticity variations and a negligible viscous moduli. Comparing QVisR elasticity estimation with VisR MSD RE estimation gCNR scores show that both simulation-trained and phantom fine-tuned QVisR better delineate an inclusion from the background. Additionally, the phantom fine-tuned QVisR model has perfect gCNR scores indicating that the 2-mm patch in the center of the inclusion is perfectly separable from the 2-mm patch outside the inclusion to the right. These results degrade only as the ROI patches approach the boundary of the inclusions and noted in Table III. Note that although it seems the VisR RE estimates [see Fig. 6(e)-(h) visually appear to more closely match the ground truth of the background material in color than the simulation-trained QVisR model [see Fig. 6(i)–(1)], the VisR RE results are on a semiquantitative scale which means an error metric for the background material cannot be calculated and, therefore, it cannot be evaluated if the VisR RE background is closer to the ground truth than the simulation-trained QVisR results. Since both the simulation-trained and phantom fine-tuned [see Fig. 6(m)–(p)] models are directly estimating the elastic modulus quantitatively, the RMSE of the background estimates can be compared to determine that fine-tuning improves the background and inclusion RMSE.

The ability of QVisR simulation-trained models to be domain adapted to scanner-acquired data in a calibrated phantom suggest model generalization would be feasible with relatively small labeled datasets. Additionally, QVisR domain adaption works best on materials in the interior range of samples, i.e., the medium stiffness materials rather than the softest or stiffest, suggesting an ideal labeled dataset would extend beyond the range of materials QVisR would ultimately be estimating in practice.

#### B. Clinical Acquisitions

As a secondary evaluation of QVisR model generalization, the simulation and phantom fine-tuned models estimated viscoelastic moduli in the gastrocnemius and rectus femoris muscles of two boys with DMD (see Fig. 7). Since fine-tuning was necessary for adaption from simulations to phantoms, the DMD dataset estimates should not be considered quantitative; however, a few labeled ROIs show promising trends.

The gastrocnemius peak displacement image [see Fig. 7(b)] has a region of high displacement bisected laterally by a streak of low displacement near the ARF focal depth (region 1). Interpreting the blue low peak displacement streak in isolation would indicate high elasticity; however, it is not possible to separate the effects of elasticity and viscosity. QVisR estimates indicate this low displacement streak is dominated by a change in viscous modulus [see Fig. 7(f) and (h) since the elasticity is relatively constant above this region [see Fig. 7(e) and (g)]. This result is supported visually by the VisR MSD RE and RV fits in Fig. 7(c) and (d); however, since the VisR results are semiquantitative, the exact values cannot be quantitatively compared. The corresponding displacement in Fig. 8 has a delayed peak, long recovery time, and minimal recovery after the first peak which also tends to happen with highly viscous materials at the focus. Additionally, the peak image lower left corner (region 2) shows two small regions of high displacement which QVisR suggests are points with higher elasticity and lower viscosity than the surrounding tissue [see Fig. 7(e)–(h)]. This could suggest a very stiff region that was displaced further by compressing the softer, more viscous tissue in neighboring regions. The displacements in this region are fairly typical of those with higher elasticity and low viscosity (i.e., rapid ascension to peak displacement, partial recovery between the two ARF pushes, and rapid peak displacement recovery as shown in Fig. 8). Comparing the simulation-trained and phantom fine-tuned model estimates shows an interplay between the elasticity and viscosity estimates. The phantom dataset had no viscosity, which biased the fine-tuned models toward estimating low viscosity. Region 1 still has a 2-3-Pa.s viscosity indicating strongly viscous features; however, the background of the phantom fine-tuned image is relatively homogeneous. Comparing the elasticity estimates pre and post fine-tuning shows an increase in detail and elasticity in region 2. This suggests the QvisR elasticity and viscosity estimates may be coupled and that a proper domain adaption dataset would need to include both elasticity and viscosity variations to reduce bias.

The rectus femoris peak displacement image [see Fig. 7(j)] has a central area with two points of high peak displacement (region 1) and a third point of high displacement near the bottom of the peak overlay (region 2). Interpreting the peak displacement images alone would indicate both regions have low elasticity. Simulation-trained QVisR indicates that the central high peak points in region 1 are driven by decreases in both elastic and viscous moduli whereas the high peak in region 2 is primarily due to a change in viscosity [see Fig. 7(o) and (q)]. After fine-tuning, the viscosity estimate variability decreases and the ROIs are only visible in the elasticity estimate image [see Fig. 7(p)]. VisR RE and RV show the elevated elasticity and viscosity in region 2; however, there is little change in

contrast in either the RE or RV images near region 1 [see Fig. 6(1) and (m)]. This could just be due to the lower RE sensitivity to changes in softer materials as seen in the similar RE values in the inclusions of Fig. 6(e) and (f). Displacements for each region (see Fig. 8) are difficult to interpret since the measurement axial depth is different (13.8 mm for region 1 and 17.5 mm for region 2) and axial depth can fairly dramatically change the shape of peak normalized displacements as shown in Fig. 1(h). Further analysis is necessary to determine cases where QVisR estimates are valid and a proper fine-tuning dataset for in vivo evaluations.

# C. QVisR Outcomes and Study Limitations

QVisR is able to estimate elastic and viscous moduli well given in silico displacement profiles and shows promise for generalization to ex vivo/in vivo applications when a limited dataset can be used to tune and validate model performance. Since QVisR uses displacements measured in the region of excitation and only selectively uses limited spatial averaging as a postprocessing procedure, the proposed model can estimate viscoelasticity with a finer resolution than methods that rely on measurement of a shear wave propagating over several millimeters.

A primary limitation of this study is the availability of quality, labeled displacement data. True point-wise viscoelastic moduli values are not currently measurable in clinical datasets. Additionally, calibrated phantoms with mechanical heterogeneities that vary both elastic and viscous moduli are an active area of research. Simulation material parameters were selected to cover a range of realistic values [4], [5]; however, simulating all variations of material viscoelasticities, geometries, and acoustic properties is not possible. Namely, this study is limited by use of a fixed, frequency-independent attenuation as well as the use of a single geometry and single background viscoelasticity for the heterogeneous simulations. The simulation imaging parameters were fixed to match those of the phantom and DMD dataset acquisitions with the VF7-3 transducer. QVisR is sensitive to variations in many of these imaging parameters, so separate datasets and models would need to be generated for imaging parameter combinations. For example, if the F/# or time between pushes in the VisR beam sequence were changed, a dataset with that imaging configuration would need to be simulated and a new QVisR model would need to be trained on the new dataset. Additionally, fine-tuning was necessary for translating a simulation-trained QVisR model to the calibrated CIRS phantom scanner acquisitions. This fine-tuning step is likely necessary due to a mismatch between simulated and scanner-acquired displacements with matched imaging configuration and material properties. Improving the match between simulations and scanner acquisitions is a topic of ongoing research and, in theory, would eliminate the need for fine-tuning once the simulation error is sufficiently small. Alternatively, a composite model could be trained with data from multiple imaging configurations where the imaging parameters could be included as features, similar to the focal depth parameter in current QVisR models; however, these composite models may be harder to train due to the large amount of data across varying imaging configurations.

Authorized licensed use limited to: N.C. State University Libraries - Acquisitions & Discovery S. Downloaded on August 19,2024 at 19:52:14 UTC from IEEE Xplore. Restrictions apply.

Expanding the breadth of the simulation datasets to encompass varying attenuation, more heterogeneous structures, and different imaging parameters may improve model generalization. Any additional parameter which could be known a priori, such as the imaging configurations, could be directly incorporated to the models as an input feature, similar to how axial depth and focal depth were treated in this study. Unknown confounding parameters, such as attenuation, could be estimated with other methods before use as an input or could be jointly estimated with elastic and viscous moduli if labels are available for a training set.

This study used a relatively simple neural network model architecture with minimal preprocessing of displacements before use as a model input. Focus on improving the model's understanding of the data and dataset information quality may yield estimate improvements. Using a model more appropriate for time-series analysis, such as a 1-D convolutional neural network (CNN) or recurrent neural network (RNN), or a dimensionality reduction technique, such as principal component analysis (PCA), may help the model efficiently extract the necessary information content from displacement profiles. Training efficiency may also be increased by use of a displacement quality factor to remove erroneous displacements or samples with high correlation. Use of a Bayesian approach may additionally allow use of labeling data with uncertainty, e.g., clinical muscle data could be parameterized by a mean and standard deviation from literature. Viscosity bias to the phantom dataset may be reducible by decoupling the elasticity and viscosity estimation into separate networks and freezing the viscosity network weights; however, this would remove any benefits from joint estimation of elasticity and viscosity. Investigation of alternative QVisR methods is ongoing.

### V. CONCLUSION

This study shows that there is a functional mapping, although potentially complex, between ON-axis displacements and viscoelastic moduli that can be learned from data. Across several million simulated displacement samples in the test set, QVisR estimates have an elastic modulus RMSE less than 2 kPa and a viscous modulus RMSE less than 0.5 Pa.s. QVisR estimates are stable in regions far above and below the focal depth (10–15+ mm) and with realistic scanner system SNRs (30-50 dB). When training on a random sampling of both mechanically homogeneous and heterogeneous displacement profiles, QVisR is able to delineate viscoelastic inclusion boundaries while maintaining similar performance in mechanically homogeneous materials. Although the simulation trained models do not generalize perfectly to phantom and clinical datasets currently, fine-tuning methods show promise for future implementations, and alternative modeling to improve generalization are under investigation.

#### **A**CKNOWLEDGMENT

The authors thank Dr. Melissa Caughey, Ph.D. for discussion of statistical methods, Dr. James F. Howard Jr., MD for assistance with clinical data acquisition, and Siemens Healthineers for in-kind support.

#### REFERENCES

- [1] R. Chivers, "Tissue characterization," *Ultrasound Med. Biol.*, vol. 7, no. 1, pp. 1–20, Jan. 1981. [Online]. Available: https://linkinghub.elsevier.com/retrieve/pii/0301562981900181
- [2] W. Rogers et al., "Radiomics: From qualitative to quantitative imaging," *Brit. J. Radiol.*, vol. 93, no. 1108, Apr. 2020, Art. no. 20190948. [Online]. Available: https://www.birpublications.org/doi/full/10.1259/bjr.20190948
- [3] R. M. Fleming, M. R. Fleming, W. C. Dooley, and T. K. Chaudhuri, "The importance of differentiating between qualitative, semi-quantitative, and quantitative imaging—Close only counts in horseshoes," Eur. J. Nucl. Med. Mol. Imag., vol. 47, no. 4, pp. 753–755, Apr. 2020, doi: 10.1007/s00259-019-04668-y.
- [4] F. A. Duck, Physical Properties of Tissue: A Comprehensive Reference Book. London, U.K.: Academic, 1990.
- [5] M. Levy, H. E. Bass, R. R. Stern, and V. Keppens, Handbook of Elastic Properties of Solids, Liquids, and Gases. San Diego, CA, USA: Academic, 2001.
- [6] Y.-C. Fung, Biomechanics: Mechanical Properties of Living Tissues. New York, NY, USA: Springer, 1993. [Online]. Available: http://link.springer.com/10.1007/978-1-4757-2257-4
- [7] I. Z. Nenadic et al., Ultrasound Elastography for Biomedical Applications and Medicine (Wiley Series in Acoustics, Noise and Vibration). Hoboken, NJ, USA: Wiley, 2019.
- [8] J.-L. Gennisson, T. Deffieux, M. Fink, and M. Tanter, "Ultrasound elastography: Principles and techniques," *Diagnostic Interventional Imag.*, vol. 94, no. 5, pp. 487–495, May 2013. [Online]. Available: https://linkinghub.elsevier.com/retrieve/pii/S2211568413000302
- [9] M. M. Doyley, S. Srinivasan, S. A. Pendergrass, Z. Wu, and J. Ophir, "Comparative evaluation of strain-based and model-based modulus elastography," *Ultrasound Med. Biol.*, vol. 31, no. 6, pp. 787–802, Jun. 2005. [Online]. Available: https://linkinghub.elsevier.com/retrieve/pii/S0301562905000943
- [10] M. M. Doyley, "Model-based elastography: A survey of approaches to the inverse elasticity problem," *Phys. Med. Biol.*, vol. 57, no. 3, pp. R35–R73, Feb. 2012. [Online]. Available: https://iopscience.iop.org/article/10.1088/0031-9155/57/3/R35
- [11] M. L. Palmeri and K. R. Nightingale, "Acoustic radiation force-based elasticity imaging methods," *Interface Focus*, vol. 1, no. 4, pp. 553–564, Aug. 2011. [Online]. Available: https://royalsocietypublishing.org/doi/abs/10.1098/rsfs.2011.0023
- [12] S. Chen et al., "Shearwave dispersion ultrasound vibrometry (SDUV) for measuring tissue elasticity and viscosity," *IEEE Trans. Ultrason.*, *Ferroelectr., Freq. Control*, vol. 56, no. 1, pp. 55–62, Jan. 2009.
- [13] J. Ormachea and K. J. Parker, "Comprehensive viscoelastic characterization of tissues and the inter-relationship of shear wave (group and phase) velocity, attenuation and dispersion," *Ultrasound Med. Biol.*, vol. 46, no. 12, pp. 3448–3459, Dec. 2020. [Online]. Available: https://www.sciencedirect.com/science/article/pii/S0301562920303902
- [14] M. R. Selzo and C. M. Gallippi, "Viscoelastic response (VisR) imaging for assessment of viscoelasticity in voigt materials," *IEEE Trans. Ultrason.*, *Ferroelectr.*, *Freq. Control*, vol. 60, no. 12, pp. 2488–2500, Dec. 2013. [Online]. Available: https://www.ncbi.nlm.nih.gov/pmc/articles/PMC4164206/
- [15] F. Viola and W. F. Walker, "Radiation force imaging of viscoelastic properties with reduced artifacts," *IEEE Trans. Ultrason., Ferroelectr., Freq. Control*, vol. 50, no. 6, pp. 736–742, Jun. 2003.
- [16] F. W. Mauldin et al., "Monitored steady-state excitation and recovery (MSSR) radiation force imaging using viscoelastic models," *IEEE Trans. Ultrason.*, Ferroelectr., Freq. Control, vol. 55, no. 7, pp. 1597–1610, Jul. 2008. [Online]. Available: https://ieeexplore.ieee.org/abstract/document/4559658
- [17] M. R. Selzo, C. J. Moore, Md. M. Hossain, M. L. Palmeri, and C. M. Gallippi, "On the quantitative potential of viscoelastic response (VisR) ultrasound using the one-dimensional mass-spring-damper model," *IEEE Trans. Ultrason., Ferroelectr., Freq. Control*, vol. 63, no. 9, pp. 1276–1287, Sep. 2016.
- [18] A. Sarvazyan, T. J. Hall, M. W. Urban, M. Fatemi, S. R. Aglyamov, and B. S. Garra, "An overview of Elastography–An emerging branch of medical imaging," *Current Med. Imag. Rev.*, vol. 7, no. 4, pp. 255–282, Nov. 2011. [Online]. Available: http://www.eurekaselect.com/openurl/content.php?genre=article&issn=1573-4056&volume=7&issue=4&spage=255

- [19] M. M. Hossain, T. Nichols, E. Merricks, and C. Gallippi, "Viscoelastic response (VisR)-derived relative elasticity and relative viscosity reflect true elasticity and viscosity, in silico," in *Proc. IEEE Int. Ultrason. Symp.* (*IUS*). Washington, DC, USA: IEEE, Sep. 2017, pp. 1–4.
- [20] C. J. Moore, M. C. Caughey, M. Chopra, J. F. Howard, and C. M. Gallippi, "Estimating degree of mechanical anisotropy in dystrophic and control rectus femoris in boys using VisR ultrasound, in vivo," in *Proc. IEEE Int. Ultrasonics Symp. (IUS)*. Washington, DC, USA: IEEE, Sep. 2017, pp. 1–4.
- [21] M. M. Hossain and C. M. Gallippi, "Viscoelastic response ultrasound derived relative elasticity and relative viscosity reflect true elasticity and viscosity: In Silico and experimental demonstration," IEEE Trans. Ultrason., Ferroelectr., Freq. Control, vol. 67, no. 6, pp. 1102–1117, Jun. 2020. [Online]. Available: https://ieeexplore. ieee.org/document/8945347/
- [22] J. B. Richardson et al., "Machine learning approaches for quantitative viscoelastic response (QVisR) ultrasound," in *Proc. IEEE Int. Ultrason. Symp. (IUS)*. Las Vegas, NV, USA: IEEE, Sep. 2020, pp. 1–3.
- [23] J. B. Richardson and C. M. Gallippi, "Effect of SNR on quantitative viscoelastic response (QVisR) ultrasound in silico," in *Proc. IEEE Int. Ultrason. Symp. (IUS)*. Xi'an, China: IEEE, Sep. 2021, pp. 1–3.
- [24] J. B. Richardson and C. M. Gallippi, "Quantitative viscoelastic response (QVisR) domain adaption with fine tuning," in *Proc. IEEE Int. Ultrason.* Symp. (IUS), Oct. 2022, pp. 1–3.
- [25] M. L. Palmeri, B. Qiang, S. Chen, and M. W. Urban, "Guidelines for finite-element modeling of acoustic radiation force-induced shear wave propagation in tissue-mimicking media," *IEEE Trans. Ultrason.*, *Ferroelectr., Freq. Control*, vol. 64, no. 1, pp. 78–92, Jan. 2017. [Online]. Available: https://ieeexplore.ieee.org/document/7792721/
- [26] J. A. Jensen and N. B. Svendsen, "Calculation of pressure fields from arbitrarily shaped, apodized, and excited ultrasound transducers," *IEEE Trans. Ultrason., Ferroelectr., Freq. Control*, vol. 39, no. 2, pp. 262–267, Mar. 1992. [Online]. Available: http://ieeexplore.ieee.org/document/139123/
- [27] G. F. Pinton, J. J. Dahl, and G. E. Trahey, "Rapid tracking of small displacements with ultrasound," *IEEE Trans. Ultrason.*, *Ferroelectr.*, *Freq. Control*, vol. 53, no. 6, pp. 1103–1117, Jun. 2006. [Online]. Available: http://ieeexplore.ieee.org/document/1642509/
- [28] C. J. Moore et al., "In vivo viscoelastic response (VisR) ultrasound for characterizing mechanical anisotropy in lower-limb skeletal muscles of boys with and without Duchenne muscular dystrophy," *Ultrasound Med. Biol.*, vol. 44, no. 12, pp. 2519–2530, Dec. 2018.
- [29] G. E. Trahey, M. L. Palmeri, R. C. Bentley, and K. R. Nightin-gale, "Acoustic radiation force impulse imaging of the mechanical properties of arteries: In vivo and ex vivo results," *Ultrasound Med. Biol.*, vol. 30, no. 9, pp. 1163–1171, Sep. 2004. [Online]. Available: https://linkinghub.elsevier.com/retrieve/pii/S0301562904001905
- [30] S. A. McAleavey, K. R. Nightingale, and G. E. Trahey, "Estimates of echo correlation and measurement bias in acoustic radiation force impulse imaging," *IEEE Trans. Ultrason.*, Ferroelectr., Freq. Control, vol. 50, no. 6, pp. 631–641, Jun. 2003. [Online]. Available: http://ieeexplore.ieee.org/document/1209550/
- [31] P. J. Huber, "Robust estimation of a location parameter," Ann. Math. Statist., vol. 35, no. 1, pp. 73–101, Mar. 1964. [Online]. Available: https://projecteuclid.org/journals/annals-of-mathematical-statistics/volume-35/issue-1/Robust-Estimation-of-a-Location-Parameter/10.1214/aoms/1177703732.full
- [32] D. P. Kingma and J. Ba, "Adam: A method for stochastic optimization," 2014. arXiv:1412.6980.
- [33] T. O. Hodson, "Root-mean-square error (RMSE) or mean absolute error (MAE): When to use them or not," Geoscientific Model Develop., vol. 15, no. 14, pp. 5481–5487, Jul. 2022. [Online]. Available: https://gmd.copernicus.org/articles/15/5481/2022/gmd-15-5481-2022.html

- [34] A. Rodriguez-Molares et al., "The generalized contrast-to-noise ratio: A formal definition for lesion detectability," *IEEE Trans. Ultrason., Ferroelectr., Freq. Control*, vol. 67, no. 4, pp. 745–759, Apr. 2020. [Online]. Available: https://ieeexplore.ieee.org/abstract/document/8918059
- [35] T. Hastie, R. Tibshirani, and J. H. Friedman, The Elements of Statistical Learning: Data Mining, Inference, and Prediction (Springer Series in Statistics), 2nd ed. New York, NY, USA: Springer, 2009.



Joseph B. Richardson (Student Member, IEEE) received the B.S. degree in electrical engineering from The University of Alabama at Birmingham, Birmingham, AL, USA, in 2019. He is currently pursuing the Ph.D. degree in electrical and computer engineering with North Carolina State University, Raleigh, NC, USA.

He is also a Graduate Student Research Assistant with the Gallippi Laboratory, Chapel Hill, USA. His current research interests include developing quantitative viscoelastic measure-

ments of anisotropic tissue using ARF-based imaging techniques and physics-constrained machine-learning model applications in ultrasound.



Christopher J. Moore (Member, IEEE) was born in Newark, OH, USA, in 1989. He received the bachelor's degrees in fine arts and electrical engineering from Ohio University, Athens, OH, USA, in 2012 and 2013, respectively, and the Ph.D. degree in electrical engineering from North Carolina State University, Raleigh, NC, USA, in 2019.

Since 2023, he has been serving as an Imaging Specialist at Revvity, Waltham, MA, USA, where he works with industry and academic

partners to identify imaging-based solutions for drug discovery and biomarker tracking.



Caterina M. Gallippi (Senior Member, IEEE) received the B.S.E. degree in electrical engineering and a certificate in engineering biology from Princeton University, Princeton, NJ, USA, in 1998, and the Ph.D. degree in biomedical engineering from Duke University, Durham, NC, USA, in 2003, with a focus on ultrasonic imaging.

She is currently a Professor with the Joint Department of Biomedical Engineering, University of North Carolina at Chapel Hill, Chapel

Hill, NC, USA, and North Carolina State University, Raleigh, NC, USA. She is also the Director of the Unified Medical Ultrasound Technology Development (UNMUTED) NIH T32 Predoctoral Training Program. Her research interests include radiation force imaging, adaptive signal filtering, multidimensional motion tracking, and magneto-motive ultrasound. Her group works to apply these novel technologies to cardiovascular disease, cancer, kidney disease, and musculoskeletal disorders.